④

AD-A213 814

DTIC FILE COPY

MEASUREMENT OF OPTICAL RADIATIONS IN SPACECRAFT ENVIRONMENTS

I. L. Kofsky
N. H. Tran
M. A. Maris
C. A. Trowbridge

PhotoMetrics, Inc.
4 Arrow Drive
Woburn, MA   01801-2057

15 June 1989

DTIC
ELECTE
OCT 3 0 1989
S E D

GEOPHYSICS LABORATORY
AIR FORCE SYSTEMS COMMAND
UNITED STATES AIR FORCE
HANSCOM AFB, MASSACHUSETTS   01731-5000

89 10 27 171

"This technical report has been reviewed and is approved for publication"

EDMOND MURAD
Contract Manager

CHARLES P. PIKE, Chief
Spacecraft Interactions Branch

FOR THE COMMANDER

DAVID A. HARDY, Acting Director
Space Physics Division

REPORT DOCUMENTATION PAGE

1a REPORT SECURITY CLASSIFICATION Unclassified		1b RESTRICTIVE MARKINGS		
2a SECURITY CLASSIFICATION AUTHORITY		3 DISTRIBUTION/AVAILABILITY OF REPORT Approved for public release; Distribution unlimited.		
2b DECLASSIFICATION/DOWNGRADING SCHEDULE				
4 PERFORMING ORGANIZATION REPORT NUMBER(S) PhM-P-06-89		5 MONITORING ORGANIZATION REPORT NUMBER(S) GL-TR-89-0168		
6a NAME OF PERFORMING ORGANIZATION PhotoMetrics, Inc	6b OFFICE SYMBOL (If applicable)	7a NAME OF MONITORING ORGANIZATION Geophysics Laboratory		
6c ADDRESS (City, State, and ZIP Code) 4 Arrow Drive Woburn, MA 01801		7b ADDRESS (City, State, and ZIP Code) Hanscom AFB Massachusetts 01731-5000		
8a NAME OF FUNDING/SPONSORING ORGANIZATION	8b OFFICE SYMBOL (If applicable)	9 PROCUREMENT INSTRUMENT IDENTIFICATION NUMBER F19628-88-C-0070		

8c ADDRESS (City, State, and ZIP Code)	10 SOURCE OF FUNDING NUMBERS			
	PROGRAM ELEMENT NO	PROJECT NO	TASK NO	WORK UNIT ACCESSION NO
	63220C	S321	31	AA

11 TITLE (Include Security Classification)
Measurement of Optical Radiations in Spacecraft Environments

12 PERSONAL AUTHOR(S)
I. L. Kofsky; M. A. Maris, N. H. Tran, C. A. Trowbridge

13a TYPE OF REPORT Scientific #1	13b TIME COVERED FROM ____ TO ____	14. DATE OF REPORT (Year, Month, Day) 1989 June 15	15 PAGE COUNT 50

16 SUPPLEMENTARY NOTATION

17 COSATI CODES			18. SUBJECT TERMS (Continue on reverse if necessary and identify by block number)
FIELD	GROUP	SUB-GROUP	Spacecraft contamination Particulate scattering
			Optical glows Water photolysis
			Radiometry.

19 ABSTRACT (Continue on reverse if necessary and identify by block number) Three topics in remote sensing of the gaseous and particulate environment of spacecraft are reported and several further optical contamination and induced-glow phenomenology issues now under consideration are briefly reviewed. The transmission to ground stations of the near-ultraviolet radiation from OH^* excited when high-kinetic energy H_2O molecules in thruster rocket exhaust react with the ambient O atoms is calculated from band and atmosphere models, and the measurement signal/noise is shown to depend on the concentrations of both (UV-absorbing) O_3 molecules and (UV sky background-producing) O atoms along the view path as well as on the spatial distribution of radiance from the exoatmospheric collision volume. Vacuum-ultraviolet photolysis of water vapor off spacecraft with radiometry of the resulting electronically-excited, microsecond-lifetime hydroxyl radicals is shown to be a feasible means for determining its rates of off-gassing, and preliminary designs for such active probes are presented. An initial review of the potential for identification of spaceborne particulates from their chemical composition-dependent scattering and emission of visible and infrared quanta indicates that synthetic (instrument response-convolved) spectra of candidate contaminant particles are needed to

20 DISTRIBUTION/AVAILABILITY OF ABSTRACT ☐ UNCLASSIFIED/UNLIMITED ☐ SAME AS RPT ☐ DTIC USERS	21 ABSTRACT SECURITY CLASSIFICATION Unclassified	
22a NAME OF RESPONSIBLE INDIVIDUAL Edmund Murad	22b TELEPHONE (Include Area Code)	22c OFFICE SYMBOL GL/PHK

DD FORM 1473, 83 MAR
83 APR edition may be used until exhausted
All other editions are obsolete

evaluate the concept. Tasks in progress including planning of the pointing of USAF's separated platform-mounted Arizona Imager/Spectrograph against the desorbed and control rocket exhaust gas volumes, gases released for scientific purposes, the surface-catalyzed recombination glows off ram of Shuttle Orbiter, and (a largely unrelated geophysical issue) the atmosphere's limb; and reduction-analysis of visible-light video images taken from groundbased and onboard of water dumps and infrared images of thruster product gases made with the large aperture telescope at the AMOS mountaintop observatory.

FOREWORD

This report documents three tasks in optical remote sensing
of spacecraft environments performed by PhotoMetrics in the first
year of Contract F19628-88-C-0070 with the Spacecraft Interactions
Branch (PHK) of USAF's Geophysics Laboratory.

Section 1 identifies the technical issues in measurement from
ground stations (that is, viewing through the lower atmosphere) of
the ultraviolet electronic-band radiation from hydroxyl radicals
produced when the high-velocity water vapor, which constitutes a
large fraction of the exhaust of several types of thruster rocket
engine, collides with the ambient atmosphere. It shows that the
optimum camera- or non-imaging radiometer-telescope depends on the
radiance distribution predicted for this reaction volume, and that
the measurement signal/noise ratio varies with the concentrations
along the view path of ozone molecules (which absorb in the UV)
and oxygen atoms (which recombine in the lower thermosphere to
form the dominant sky background at the radiometry wavelengths).
Section 2 presents a preliminary design for "active" measurement
of the concentrations of offgassed (and exhaust-related) H_2O
molecules, from the short-lived electronically excited OH product
of photolysis by VUV photons from a resonance lamp onboard the
space vehicle; the approach is shown to be sensitive to the rates
of water vapor emission that have been previously inferred by
other methods (principally, mass spectrometry). Section 3 is a
review of the potential of measurements of sunlight-scattering and
thermal-emission spectra from the microns-scale particulate
contaminants that frequently appear near spacecraft for
identifying the sources of these particles; it concludes that
compiling a synthetic database of such spectral distributions for
candidate particle compositions (and dimensions) convolved with
the response of realizable filter cameras and wavelength-
dispersing instruments (such as the USAF's Arizona
Imager/Spectrograph (AI/S)), is the next step in development of
this concept.

Several other issues in inadvertent optical contamination of spacecraft environments and the phenomenology of the UV-visible-IR glows that result from purposeful (scientific experiment-related) and housekeeping (control rockets, water dump) sources are currently being addressed. Principal among these are the following.

1) Planning of the pointing program of the AI/S from a subsatellite platform (the SPAS) that will lead Shuttle Orbiter by a few km. This multichannel ultraviolet- and visible light-sensitive instrument is scheduled to measure surface radiances of the rocket exhaust plumes, gas releases (some of which are intended to test the Critical Ionization Velocity hypothesis, and thus could result in structured ion clouds), outgas contamination, and recombination glows catalyzed by spacecraft areas exposed to the impinging atmosphere, as well as altitude profiles of the dayglow and nightglow emission from the atmosphere's limb, all in conjunction with an infrared radiometer array and spectrometer (the IBSS) essentially coaligned with it.

This effort includes preparation of two-dimensional projections to the remote instrument platform that show the vehicle in its series of planned orientations during the mission, with overlays of the fields of view of the wide- and narrow-angle interference filter cameras and (one-dimensional-imaging) spectrograph. These views are based on a "true" three-dimensional computer model of the outline of Shuttle Orbiter that we developed in connection with the Drafix[R] projection program, which has the capability of rejecting geometric features that lie hidden behind opaque areas closer in the line of sight. We also made an analog simulation of the views of Orbiter's body from SPAS by photographing a scale model illuminated by an incandescent lamp ("the sun") at several elevation-azimuth angles, with a camera at the scaled separation having the same angular field(s) of view as the Arizona Imagers. Completion of the set of digital computer projections of Shuttle Orbiter and the optical glows from the space around it awaits finalization of its three-axis aspect at

the times of reaction control engine burns and chemical releases.

2) Planning of remote ultraviolet and infrared (0.3-20 μm) radiometry of the H_2O molecules outgassed from, purposefully ejected from (for example in venting of waste water), and produced in the engine burns of Orbiter. A wide range of uncertainty exists in the input parameters for prediction of the intensities of these optical emissions. At issue are the rates of outgassing, which vary among as well as during individual flight missions (the existing data are not in good agreement); the spatial distributions of water vapor that result from collisions with the atmosphere in the ram direction at the lower shuttle orbital altitudes; and in particular the cross sections for impact excitation of $H_2O^\dagger$ and $OH^{*,\dagger}$ when water molecules moving at greater than orbital velocities collide with the atmosphere's oxygen atoms (refer to Ref 1), as well as the rotational widths of these electronic and vibrational bands (see Section 1). The spreads of values of these parameters will be taken into account in planning characterization of these contaminant glows. We are in the process of scoping the pattern of radiant intensities in the fields imaged by AI/S and IBSS operating from SPAS in the same circular orbit (and thus directed horizontally).

Pending receipt of more accurate scene radiances from computer models of the exhaust and outgassing (such as the CHARM code), we are using the simple distribution of outgas applied in a recent report (Ref 8) to estimate with manual calculations the distribution of infrared and ultraviolet column intensities in projections to SPAS. The noise-equivalent radiances of the optical sensors are

IBSS SWIR-MWIR radiometers :   5 x 10^{-9} W/cm^2 ster (in band)
IBSS spectrometer   :   8 x 10^{-7} W/cm^2 ster μm
AI/S sections (approximate): 10^{-11} W/cm^2 ster (in band, or per ~30 A).

Should the infrared radiances from water vapor (corrected for the view angle from SPAS) be comparable with the 10^{-9} W/cm^2 ster figure for outward-viewing projections estimated in this report,

they would be detected by the radiometers; in contrast, unexpectedly large water vapor outgassing rates, or enhancements of concentration from backscattering off the windward orbital atmosphere, would be needed to bring the signal up to the much higher measurement threshold of the IBSS spectrometer.

We are considering UV as well as the SWIR-MWIR-LWIR radiations that result from solar pumping and earthshine pumping, and (principally) collisional excitation; this last mechanism is the direct impact population of both H_2O $(\nu_1\nu_2\nu_3)$ and OH (A, and $v>0$, and $J>0$) when H_2O molecules are incident with super-orbital relative velocities on N_2 molecules and O atoms. The reaction $O + H_2O \rightarrow OH^{*,\dagger} + OH$ is discussed in Ref 1, where theoretical cross-sections for population of OH(A) and OH (X, $v>0$) are derived. (The reaction also plays a part in Section 1 of this Report.)

The planning calculations for measurements of these emissions with AI/S-IBSS include the following phenomena.

a) Production of OH in the energetically-accessible upper electronic levels of ultraviolet transitions to which the AI/S is sensitive (the A $\rightarrow$ X 0,0, 0,1, 1,0, 1,1, ... bands near 3000 A; see Section 1).

b) Resonant and fluorescent scattering of sunlight and earthshine from these hydroxyl radicals (presumably a small effect; estimates of the ultraviolet radiance require some estimate of [OH] in the vicinity of the space vehicle, as transfer of kinetic energy to OH accompanying the dissociation of H_2O causes the species to move much more rapidly out of the sensor field than the outgassed water molecules).

c) Excitation of the 100 $\rightarrow$ 000, 101 $\rightarrow$ 000, 001 $\rightarrow$ 000 and 011 $\rightarrow$ 000 bands of H_2O, as well as LWIR from rotational excitation of H_2O and OH.

d) Radiations from thruster rocket engine exhaust (see Ref 1 and Section 1).

e) Background noise from leakage through the sensor telescopes of

optical radiations from nearby Orbiter and from the atmosphere
(see below).

f) The effect of sight projections passing tangential to Orbiter
surfaces (refer to Section 5 of Ref 1 for a review of the apparent
radiances in radial and tangentially-passing views).

Leakage of out-of-field photons results in an increase in
effective noise equivalent radiance (or spectral radiance) of the
IBSS radiometers in projections that pass within a few degrees of
Orbiter's body, as has been shown by a recent (unpublished) study.
We are calculating the similar artifactual signal for AI/S from
the initial specification of the out-of-field rejection of its
telescopes, applying an estimated diffuse visible and ultraviolet
albedo of its tile surfaces and the known spectral radiance
profile of the sunlit atmosphere below the horizontal line-of-
sight from SPAS. We are also applying the celestial background--
as is done in Section 2 (and to some extent Section 1) for the
measurement of the ultraviolet radiation from OH^*--to estimate the
signal/noise ratios of the several IR and UV emissions from H_2O
and OH molecules off spacecraft surfaces.

3) Preparation of a technical-journal article reviewing the
UV-visible-IR glows that have been observed when incident
atmospheric atoms and molecules recombine on the surfaces of low
earth orbiting spacecraft or sounding rockets exposed to the
airflow, and excited by broadly-related processes involving
energetic atmospheric and substrate/adsorbed species. To date we
have identified some 60 literature references on this topic. The
focus of this article is the optical "foregrounds" that interfere
with surveillance and geophysical/astronomical measurements from
space platforms.

4) Reduction, analysis, and interpretation of a) groundbased
(AMOS 22-inch finder telescope) and onboard (by two zoom cameras,
one handheld in the crew cabin and the other mounted in Orbiter
Discovery's bay near its vertical stabilizer) video images of the
visible sunlight scattered from the ice particles that result from

venting of fuel-cell product water, and b) groundbased (AMOS main telescope) staring infrared detector array images of the exhaust gases from pulsed Orbiter reaction engine burns. We are extracting photometric and photogrammetric information from these images with a video processing system that converts them into contour maps and line plots of radiance along the long and transverse axes of the glows. The sunlight-scatter glow from the water-dump trail is optically thin, and its peak radiance (along its long axis) in projections to the ground station while the lower atmosphere is in darkness decreases increasingly rapidly beyond about 100 m from the nozzle; this behavior is consistent with evaporation of Rayleigh-scattering particles (circumference less than the mean light wavelength). These images of the two types of extra-vehicular glow from shuttle mission STS-29, taken in an experiment designed and executed by Geophysics Laboratory, carry important information about the optical signatures of potential spacecraft-obscuring materials.

TABLE OF CONTENTS

LIST OF TABLES

LIST OF ILLUSTRATIONS

GROUNDBASED MEASUREMENT OF HYDROXYL ELECTRONIC BAND RADIATION FROM ROCKET ENGINE EXHAUST PLUMES

Introduction

Hydroxyl radicals in their first electronically excited state are expected to be one of the principal radiative species produced when ram-directed exhaust gas from monomethyl hydrazine fuel-nitrogen tetroxide oxidizer (and other) thruster engines collides with atmospheric oxygen near low earth-orbiting spacecraft and re-entry vehicles. As is detailed in Section 6 of Ref 1, water molecules constitute a major mole fraction of the exhaust products from such engines, and their excitative reaction with oxygen atoms (the most abundant ambient species)

$$H_2O\ (\tilde{X}^1A_1) + O^3P \rightarrow OH\ (X^2\Pi,\ v=0) + OH\ (A^2\Sigma^+,\ v=0)$$
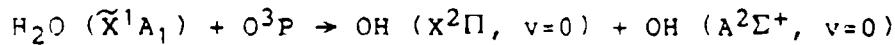
is up to ~1½ eV exothermic as well as being spin conservation-permitted. The branching ratio for the transition

$$OH\ (A,\ v=0) \rightarrow OH\ (X,\ v=0) + h\nu\ (R\ branch\ bandhead\ at\ 3064\ \text{Å})$$
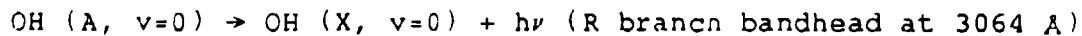
is 0.9. Since the radiative lifetime of the excited hydroxyl radicals is 1 microsecond they move only a negligible distance from where they were created, and thus accurately map the reaction volume.

A capability to verify DoD computer models of the electronic excitation of OH in the high-velocity thruster exhaust from groundbased measurements of the surface radiance distribution (or even sterance) of this volume would represent a substantial cost saving over measurements from rocketborne platforms. We present here an initial review of the technical issues in such remote sensing. As we will show, estimates of the absolute spatial yields of this hydroxyl radiation--which

1

are forthcoming from these code models--are needed for a final design of the ground-based imaging or radiometry system.

Technical Issues

The near-ultraviolet A → X band is strongly Rayleigh- and Mie-scattered by molecules and aerosols in the troposphere, and furthermore lies very close to the long-wavelength limit of the Hartley-bands absorption by the ozone molecules present principally in the stratosphere. In consequence ground stations that are frequently above the inversion layer, below which most of the atmospheric particulates are confined, would be favored. We therefore perform the model transmission calculations that follow for the Air Force Maui Optical Station (AMOS), at 3049 m, approximately 21°N and 204°E, where the nighttime seeing conditions are usually very good (the ocean cloud deck tends to be below the isolated mountaintop) and where several high throughput, precisely radar-tracked telescope-cameras are located. We consider the "best case" of measurements against the moonless night sky (solar depression >18°, after astronomical twilight) with the exhaust-producing vehicle in the zenith; the procedure of course applies directly to other elevation angles of the orbiting spacecraft or non-ballistic re-entry body. As noted, the application of specific sensors--that is, prediction of the resulting optical signal/noise ratios-- requires the aforementioned absolute yields and distribution in angle from the station of the hydroxyl emission produced by designated types of thruster engine.

The following factors figure in measurement of the plume radiation transmitted to the sensor above the optical noise from atmospheric and astronomical sources and due to dark current of its photodetector.
   -- Spectral distribution within the electronic band, which is broadly spread due to its mode of excitation;
   -- transmission of the [zenith] atmosphere;
   -- background radiance of the dark night sky;   and

2

-- spectral response of the groundbased camera or photometer.
Figure 1 shows the first three of these parameters, along with
the effect on the photocurrent signal of varying the wavelength
of maximum transmission of a "perceivedly-best" ultraviolet
filter (discussed further below).

Spectral Distribution of the Radiation Source

The spectral distribution within the OH A $\rightarrow$ X bands from
the excitative reaction has not been measured, or calculated.
The widths of the P, Q, and R branches in Figure 1--which we
have approximated with essentially "top hat" shapes--are
estimates from the rotational development calculated for the
somewhat analogous collisions of ~eV's kinetic energy oxygen
atoms that result in vibrational and/or rotational excitation of
water and hydroxyl molecules:

$$O + H_2O \ (000) \quad \rightarrow \ H_2O \ (000, \ \nu_1\nu_2\nu_3) + O \quad (\text{Ref's } 2,3)$$
$$O + OH \ (X, \ v=0) \rightarrow OH \ (X, \ v>0) + O \qquad (\text{Ref } 4).$$
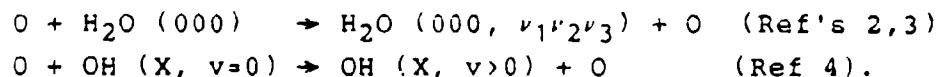
The effective rotational "temperature" of the OH electronic band
is very approximately ½ eV. This estimate is supported by the
argument that when the H_2O_2 intermediate product of the $O + H_2O$
reaction splits up, comparable energy goes into rotational and
translational modes of the two OH radicals. In any case the
total transmission of the hydroxyl band radiation through the
lower atmosphere can be seen in Figure 1 to be relatively
insensitive to its (collisionally-averaged) spectral
distribution.

Transmission to the Telescope

The critical variable in transmission of these photons with
wavelengths just above 3064 A is the atmosphere's column
density of O_3 molecules. We took the total ozone density above
AMOS to be the seasonally-averaged value at the latitude and
longitude of Hawaii (from Ref 5), 0.275 atmosphere-cm, reduced

3
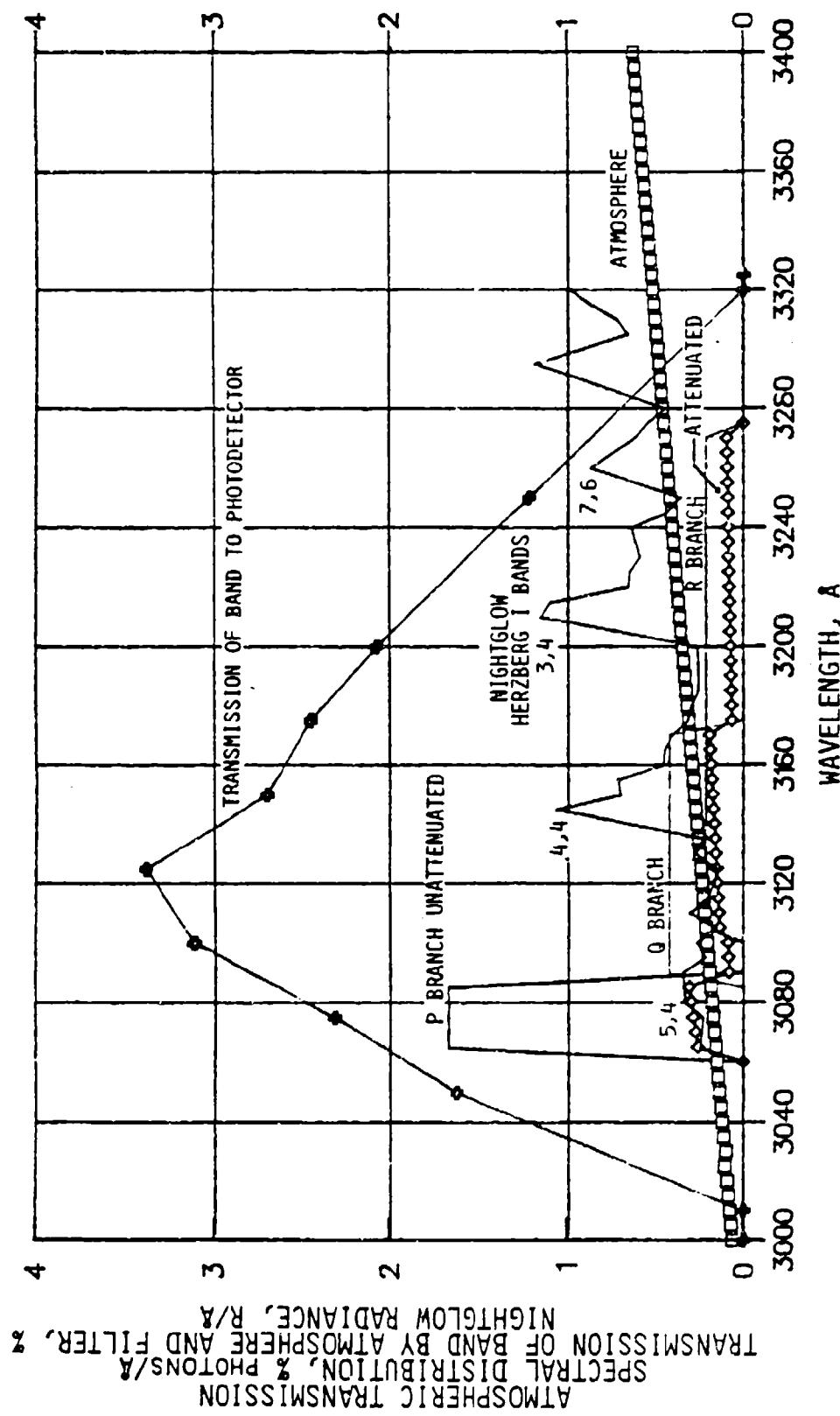
Figure 1. Transmission of the zenith atmosphere above AMOS (refer to the text for assumptions about column-concentrations of ozone and aerosols), model spectral distribution in the OH $0,0$ A $\rightarrow$ X band, nightglow radiance from Ref 7, and relative incident and signal irradiances with 100 Å FWHM interference filters having 20% maximum transmission at the wavelengths indicated. Some O_2 Herzberg I airglow bands are identified.

by 12% to take into account the vertical-column density in the troposphere below the 3 km altitude of the station (derived from the $[O_3]$ altitude profiles in Ref 5, which in fact refer to a broader latitude range). The variation about this annual mean is only about 7% at the low latitude of AMOS, and in any case the mean seasonal value could be applied to predict the attenuation in the projected month of an actual exhaust plume radiation measurement. This column density transmits very closely 50% of the zenith radiation at 3100 Å.

We assume also the relatively standard maritime tropical atmosphere with 23-km visibility at sea level from LOWTRAN 6 (Ref 6). The resulting Rayleigh-molecular outscattering is $(1 - 0.47)$ at 3100 Å; and the particulate scattering is $(1 - 0.89)$ over most of the hydroxyl emission wavelengths shown in Figure 1, which means that the effect of error in the actual aerosol loading of the atmosphere above AMOS would be small. The net transmission of the zenith atmosphere from LOWTRAN 6 is 0.153 at the 3064 Å bandhead, rising to 0.458 at the adopted 3275 Å long-wavelength "limit" of the P branch. When the exhaust plume is at 30° zenith angle from the ground station--a presumably more common measurement condition--these atmosphere transmissions decrease to 0.115 and 0.406 respectively.

Sky Background

Nightglow from the out-of-chemical equilibrium upper atmosphere is the dominant sky background when no individual bright UV stars are in narrow sensor fields of view. The intensity data illustrated in Figure 1 (Ref 7) were taken from a latitude ~10° higher than Hawaii, with a 5 Å FWHM spectrometer at 2100 m altitude pointed near the zenith and toward the galactic pole to minimize the stellar background. (UV zodiacal light, or sunlight at modest solar elongations reflected off dust particles principally in the ecliptic plane, is substantially weaker at ground stations than this airglow; refer also to later Table 2.) As these data are uncorrected for

atmospheric extinction--which is principally by ozone absorption, since a large fraction of the Rayleigh-scattered photons from the full-sky radiating source reach the ground-- they represent, with the caveat stated immediately below, the spatially-continuous background presented to AMOS telescopes viewing near the galactic pole.

Virtually all of this ultraviolet radiation is in Herzberg I bands of $O_2(A^3\Sigma_u^+ \rightarrow X^3\Sigma_g^-)$, most of which are identified in Figure 1. $O_2(A)$ molecules are excited by recombination of O atoms, the concentrations of which at the principal nightglow-emission altitudes near 100 km are known to vary with latitude as well as with solar activity and related geophysical parameters. These changes in the [O] profile are evidenced by the natural global and temporal variability--over a dynamic range of at least a factor 10--of the column intensity of the airglow in the OI $^1S \rightarrow {}^1D$ green line at 5577 Å. This feature is similarly excited, at the same lower-thermospheric altitudes, by recombination of O^3P atoms, and the Herzberg-bands airglow is known to correlate with it. A range of perhaps a factor four in the intensity of these $O_2 A \rightarrow X$ bands could be expected at an individual ground station at the low latitude of AMOS, where the variability in the oxygen atom profile tends to be less than towards the poles.

While no systematic data are available on the statistics of the Herzberg I bands nightglow over Hawaii, estimates of this UV background intensity at the time of planned measurements of rocket-exhaust radiations could be made from straightforward models that scale the results shown in Figure 1--for which the geophysical conditions are largely known--to the profiles of [O] predicted by MSIS (or other models of upper-atmospheric species concentrations). Alternatively, measurements of the absolute UV airglow radiances at AMOS, supported--perhaps even supplanted-- by similar observations of the OI green line, could be applied to refine the sky background intensities shown in Figure 1.

(If the background of the night sky turns out to be the

6

factor dominating in the signal/noise ratio, the exhaust plume
measurements would best be scheduled for the hours during which
the star-poor galactic pole lies near the zenith of the ground
station.)

Sensor Response

The spectral response of the imaging or single-channel
photometer (assuming uniform response of the reflecting AMOS
telescope) depends principally on the design of its wavelength-
isolating filter. The small variation with wavelength near
3100 Å of the quantum efficiency of quartz-window S-11 or other
commonly-used bialkali type photocathodes can be neglected for
planning purposes. (The change is about 10% between 3064 Å
and 3260 Å, over which range the mean photoconversion yield is
0.2; in contrast "solar blind" CsTe photocathodes exhibit yields
of only about 0.01 with a strong variation over the hydroxyl
band, albeit very low dark count rates).

While the total number of 0,0-band photons reaching the
photocathode quite obviously increases with the spectral width
of the filter (refer to Figure 1), the leakage of sky background   .
radiation also increases. Narrowing the bandpass generally
reduces the maximum transmission (an effect inherent to multi-
cavity interference filters), and is usually accompanied by
increased out-of-band transmission, in particular at visible
wavelengths where the spectral radiance of airglow plus
celestial sources is greater than in the vicinity of the
ultraviolet hydroxyl band. The choice of widths is dictated by
the availability of commercially-fabricated such filters, which
near 3100 Å are made with FWHM's extending upward from ~55 Å
(for example the Series XN type from Acton Research Corp. (MA)).

The statistical signal/noise ratio of the photometer, or in
individual picture elements of a camera, is in effect

$$\frac{\text{number of counts from the exhaust plume (i.e., signal counts)}}{(\text{signal counts} + 2\ [\text{background counts} + \text{dark counts}])^{1/2}},$$

where we have assumed that the mean background plus dark count

from the photocathode can be subtracted from the total number of photoelectrons counted when the radiating volume is in the telescope's field of view. A clear specification of 1) the radiance or sterance of the plume in the hydroxyl band, 2) the etendue (lens area times solid angle subtended) of a pixel or a non-imaging telescope-photometer, and 3) the dark current of the focal-plane detector, is thus needed to predict the signal/noise ratio achievable in a given integration time. Planning data on the spatial extent and sterance or peak radiance of the exhaust reaction volume [from sources such as CHARM] serve in setting the etendue of the ultraviolet sensor--that is, its angular field and thus the irradiance from the essentially spatially-continuous sky background--, and selecting the physical dimensions of the focal plane detector--on which in turn its dark current(s) depend. At the same time these parameters and the spectral radiance of the sky background determine the bandpass of the UV sensor--: narrow if rejection of sky noise is the major experiment consideration, wide if the surface radiance or sterance of the thruster exhaust volume is the factor controlling the signal/noise ratio.

Pending availability of this information about the source of emission, we can calculate a scaled signal from the hydroxyl band radiation transmitted by the atmosphere and [commercial interference filter. As Figure 1 indicates, selection of a FWHM is not intuitively obvious; for example a 55 A filter centered near 3125 A would isolate the Q branch against the gap in the Herzberg-band spectrum, while 200 A near 3150 A would encompass virtually all of the band radiation. The plot in Figure 1 of response to the transmitted spectral irradiance refers to 100 A FWHM filters (Acton Series VN, or Andover Corporation (Salem NH) Type 7) which have peak transmission at the wavelength indicated. This response exhibits a relatively flat maximum between 3100 A and 3140 A, a span within the specified manufacturing tolerance (+30, -0 A).

The response characteristic in Figure 1 was calculated with

8

a peak filter transmission of 20%, as specified by the manufacturers. We have neglected the effect of off-axis rays on the overall transmission characteristic of the interference filter, as the cone of light in the AMOS telescopes is relatively narrow and thus the resulting mean shift of transmission toward shorter wavelengths is small compared with the FWHM. (The filter quite obviously must be located in the converging beam of telescopes with objective lenses as large as those at AMOS.) For example if the main telescope or the smaller-aperture acquisition unit is operated at f/4, the largest incidence angle on the filter (which would be located near the focal plane) is 7°, at which angle the change of wavelength of peak transmission would be less than -20 A--well less than the 100 A FWHM adopted. We note that the leakage of available ultraviolet filters at visible wavelengths, where the perceivedly otherwise best photocathode type (S-11) has high quar' . efficiency and where the spectral radiance of the night sky is about a factor two or more higher than in the region shown in Figure 1, must also be taken into account in the final design of the groundbased hydroxyl-band sensor; this issue also awaits prespecification of the characteristics of the ultraviolet source.

Discussion

The above review indicates the importance for planning groundbased optical measurements or model calculations of (or interpretation of existing data from space platforms in terms of) the spatial extent and peak or mean radiance of the hydroxyl electronic band emission in the thruster exhaust plume. This information applies not only in assessing the signal "intensity" but also the ultraviolet night sky background that contributes to--and may dominate--measurement noise. (In practice no fully satisfactory photocathode exists for the wavelength region near 3100 A: CsTe has very low quantum yield, while S-11 has higher dark current even when cooled.) The actual background scene

radiance is at present uncertain, to within perhaps ±50%, due to the lack of firm data on the intensities of the O_2 Herzberg I-band airglow at Hawaii. This gap could be filled by relatively inexpensive ground measurements, should finalized exhaust plume planning results indicate the need (that is, if airglow is the principal noise source, and the overall signal/noise ratio is marginally useful).

Our analysis shows that a photometer or camera fabricated with commercially available 100 A-FWHM interference filters would count up to

[4% of the OH 0,0 A → X band photons from the exhaust plume initially directed into its field of view] x

[its transmission other than that of the filter] x

[the quantum efficiency of its photocathode].

The calculation indicates the optimum wavelength of the peak transmission of this particular filter type for the (relatively reliable) model atmosphere above AMOS and (still questionable) model spectral distribution within this electronic band. Similar calculations for other filter FWHM's would identify the center wavelength that results in maximum signal/noise for exhaust plumes with predicted absolute UV surface radiance distributions.

MEASUREMENT OF RATES OF DESORPTION OF WATER MOLECULES FROM SPACECRAFT BY ULTRAVIOLET PHOTOLYSIS

Introduction

We estimate here the radiances in the 3064 A-bandhead (0,0) transition from hydroxyl radicals in their first electronically excited state (further discussed in Section 1) that can be achieved by photolyzing some fraction of the H_2O molecules that have been desorbed or otherwise released from spacecraft and sounding rockets. We then compare these brightnesses with the celestial background and the threshold response of remote sensors such as the Air Force Geophysics Laboratory-sponsored Arizona Imager/Spectrograph (AI/S; Ref 1), to assess the potential of this active method for measuring the concentrations of water vapor near space vehicles. This process is (compare page 7)

$$H_2O + h\nu \ (\lambda < 1357 \ A) \rightarrow OH^* \ (A^2\Sigma^+, \ v \approx 0) + H$$

$$OH \ (A, \ v = 0) \rightarrow OH \ (X, \ v = 0) + h\nu \ (\lambda = 3064 \ A \ [+\sim 40 \ -0 \ A]).$$
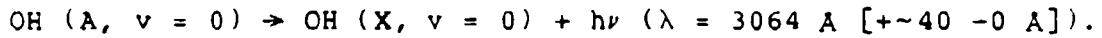
Our overall conclusion is, that water outgas rates greater than roughly 1 milligram per second from 1 meter-radius space vehicles are detectable with cameras or photometers of the scale of the AI/S with the vapor cloud illuminated from onboard by commercially-available vacuum ultraviolet light sources.

Experiment Parameters

The parameters that we adopted for these measurement-scoping calculations, along with their identifying symbols, are listed in Table 1.

We approximate the spacecraft (or sounding rocket) as a sphere of radius $z_0 = 1$ m, and assume for the initial calculation that water vapor is desorbed from this vehicle at a constant rate

Table 1. Experiment Parameters and Assumptions

1) Rate of desorption of H_2O molecules from the spacecraft* $M = 10^{21}$ sec^{-1}

2) Effective radius of the spacecraft $z_o = 100$ cm

3) Velocity of the ejected water molecules (surface at 300K)** $v_e = 5.9 \times 10^4$ cm sec^{-1}

4) Cross section for excitative photolysis of H_2O at 1236 A* $\sigma = 9.5 \times 10^{-19}$ cm^2

5) Transition probability of OH $(A \rightarrow X)$ $A = 1 \times 10^6$ sec^{-1}

6) Branching ratio of OH $(A, v=0 \rightarrow X, v=0)$* $B = 0.9$

7) Power output of the 1236 A Krypton lamp* $M_p = 10^{14}$ photons sec^{-1}*

8) Divergence of lamp beam (full angle) $\gamma_l = 20°$

9) Area of the sensor objective lens* $a_s = 0.3$ cm^2

10) Noise equivalent radiance of sensor: (All pixels coadded, 1-sec integration time)   NER $= 2 \times 10^{-14}$ W cm^{-2}ster^{-1}

11) Spectral bandpass of the sensor (full width), peak transmission* $\Delta\lambda = 55$ A, 0.20.

----

*Quantities to which the hydroxyl radiances and photometer signals calculated here are directly proportional. **Inversely proportional.

12

$M = 10^{21}$ molecules/sec $= 0.03$ gm/sec uniformly into each $[2\pi$ ster] hemisphere (first two items in Table 1). This nominal figure follows from the analysis of Shuttle Orbiter mass-spectrometer results under "steady-state" flight conditions--mission elapsed time >24 hours, with no water dumps or thruster firings taking place (Ref 8). Other estimates of Orbiter outgas rates range from ~ 0.006 gm/sec (Ref 9, also from mass-spectrometer data) to ~ 0.2 gm/sec (Ref 10, from infrared data). Since the signal in the OH band is strictly proportional to this rate at which the vehicle desorbs H_2O molecules, the results obtained here can be linearly scaled to other than the 30 mg/sec that we have adopted.

We assume (third item) that the temperature of the outer surface of the space vehicle is 300K, and that the water molecules are thermalized with this surface before they desorb. The mean velocity of effusion v_e of mass-18 species is then 5.9×10^4 cm/sec (see Section 5 of Ref 1). As this velocity is proportional to the square root of the actual surface temperature, error in this temperature has only a small effect on the ultraviolet brightnesses. Since hydroxyl radicals created with velocity a few times v_e--which would be the case if most of the excess energy of the dissociation goes i to translational motions--move on the average less than 1 mm relative to the spacecraft before emitting a 3064 A-band photon (as we already noted in Section 1), any spatial smearing of the emitted light due to transport after excitation can be ignored. The probability of a collision of 1 μsec-radiative lifetime OH^* (Ref 11) with an atmospheric atom or molecule is utterly negligible, and the orbital altitude is under most conditions high enough that collisions of desorbed H_2O molecules or ambient species before they become photolyzed can also be ignored. (This altitude is roughly 275 km for the windward direction, and all stable orbital altitudes for other directions in which $[H_2O]$ would be probed; in any case, ram enhancement _increases_ the signal/noise ratios calculated here.)

The highest-sterance photolyzing lamp that we were able to

identify in a literature survey is the Resonance Ltd. (Cookstown, Ontario) Krypton line source (seventh and eighth items in Table 1), which delivers 10^{14} 1236 Å photons/sec into an approximately 20° full angle cone (with the help of some further focusing; see Figure 2). Fortuitously, the photoabsorption cross section of H_2O has a local maximum near 1236 Å (Ref 12). Since the photolysis signal is strictly proportional to the rate of emission of 1236 Å photons, the results here can be readily scaled up should a VUV source with higher power output (or sterance) be later identified. These photons are confined to within a few Å (the lamp is an atomic resonance line source), over which range the excitative-photolysis cross section σ is (5%) $(1.9 \times 10^{-17} \text{ cm}^2)$ (Ref 12). The branching ratio B into the OH (X, v = 0) state is 0.9, as mentioned in Section 1. As the photolysis process results in little angular momentum being imparted to the OH fragment, its rotational development would be similar to that of the parent H_2O molecule at 300K. The P branch thus can be considered to extend less than about 40 Å to the red from the bandhead at 3064 Å (compare Figure 1, where the atomic collision results in much more rotational development).

We perform the signal/background calculations for the wide-field (~17° x ~18°) AI/S cameras (ninth and tenth items in Table 1), with the recognition that the design of these existing instruments may in fact not be optimum for measuring the hydroxyl glow intensities. The procedure of course directly applies to other imaging systems, and of course to non-imaging photometers with comparable focal lengths, which we discuss briefly later. The area a_s of the objective lens of these AI/S cameras is 0.3 cm^2, and the stated noise equivalent radiance (NER) for each individual 3 x 3-pixels element is to a good approximation 1×10^{-12} W/cm^2-ster, in 1-sec integration time. These cameras become single-channel photometers when all the 128 x 144 pixels of the full focal plane array are coadded, a useful operation mode when the solid angle of the induced UV glow overfills their field of view. Assuming negligible noise correlation between picture elements,

14

VUV Continuum Sources

Lamp Type	Wavelengths of half power points		VUV Irradiance at 10 cm ($\mu W/cm^2$)	VUV Flux (photons/sec/sr)
Ar/MgF$_2$	123.7	133.5	6	4 ×10E14
Kr/MgF$_2$	139.5	155.0	49	3.5×10E15
Xe/MgF$_2$	146.5	179.7	102	8.5×10E15
Xe/Qtz	165.3	179.7	23	2 ×10E15
D$_2$/Qtz	155.0	450.0	14	2 ×10E15

Molecular Sources

Lamp Type	Wavelengths (nm) partial list	Typical Flux (photons/sec/sr)
OH	(0,0) band at 306.4	1.5×10E14
NO	NO gamma bands from 180-280	4 ×10E14
CO	CO 4th Positive bands from 113-140	1 ×10E14

(a)

Optically Thin Line Sources

Lamp Type	Wavelength (nm) (partial list)	Typical Flux (photons/sec/str)
Cl	118.9	5×10E12
N	120.0	5×10E12
	149.3	
	174.3	
	LBH bands	
O	115.2	
	130.2	5×10E13
	135.6	
	777.4	
	844.6	
D	121.5	10E14
H	121.6	10E14

Rare Gas Line Sources

Lamp Type	Wavelengths (nm) (partial list)	Typical Flux (photons/sec/str)
Ar	106.0	>10E13
	733.4	>4×10E13
	763.5	
Ne	630.4	>10E13
Kr	123.6	10E15
	557.0	>10E13
Xe	147.0	10E15
Ne	630.4	>10E13
He	1083.0	>10E15

(b)

Relative UV output as a function of angle from the lamp axis

Figure 2. Characteristics of VUV lamps. a) general; b) angular radiation pattern.

15

the combined NER for the AI/S serving as a "photometer" is then $(1 \times 10^{-12}$ W/cm^2 ster$)/(128 \times 144/3 \times 3)^{1/2} \approx 2 \times 10^{-14}$ W/cm^2 ster.

To maximize signal-to-(scene) noise the focal plane of the camera could be shaped to the transverse projection of the water vapor volume irradiated by the VUV resonance lamp. Alternatively, the acceptance angle-defining slit of a photometer could be similarly shaped. Figure 3 depicts the excitation and sensing geometry. ("Transverse" here means into and out of the plane of Figure 3.) An essentially rectangular sensor field-of-view would be effective, with transverse angle $\sim \gamma_s$, while the longitudinal angle γ_1 can be increased to improve the etendue while still underfilling the projection of the excitation volume (more on this point below).

Finally (eleventh item in Table 1), we adopt for the camera system the commercially-available spectral FWHM of 55 A centered somewhat longward of the OH A $\rightarrow$ X 0,0 R branch head at 3064 A. (Refer again to the general shape of the electronic band in Figure 1.) We apply the simplifying approximation that the filter passes the complete band, with a transmission of 20%. The "XN" series interference filters made commercially by Acton Research Corp. (Acton MA)--guaranteed peak-transmission wavelength tolerance <25% of this FWHM, and peak at least 10%--appear best suited to this application (despite the tendency of this filter design to exhibit finite transmission at near-UV and visible wavelengths, an effect not considered here).

Radiance Signal

The number density n of water molecules at distance z from the geometric center of the spacecraft is

$$n = M/2\pi v_e z^2$$

(where the extremely small depletion of the H_2O "beam" by the pumping light is ignored). Similarly, the number density n_p of 1236 A photons within the illumination cone at distance x_1 from

16
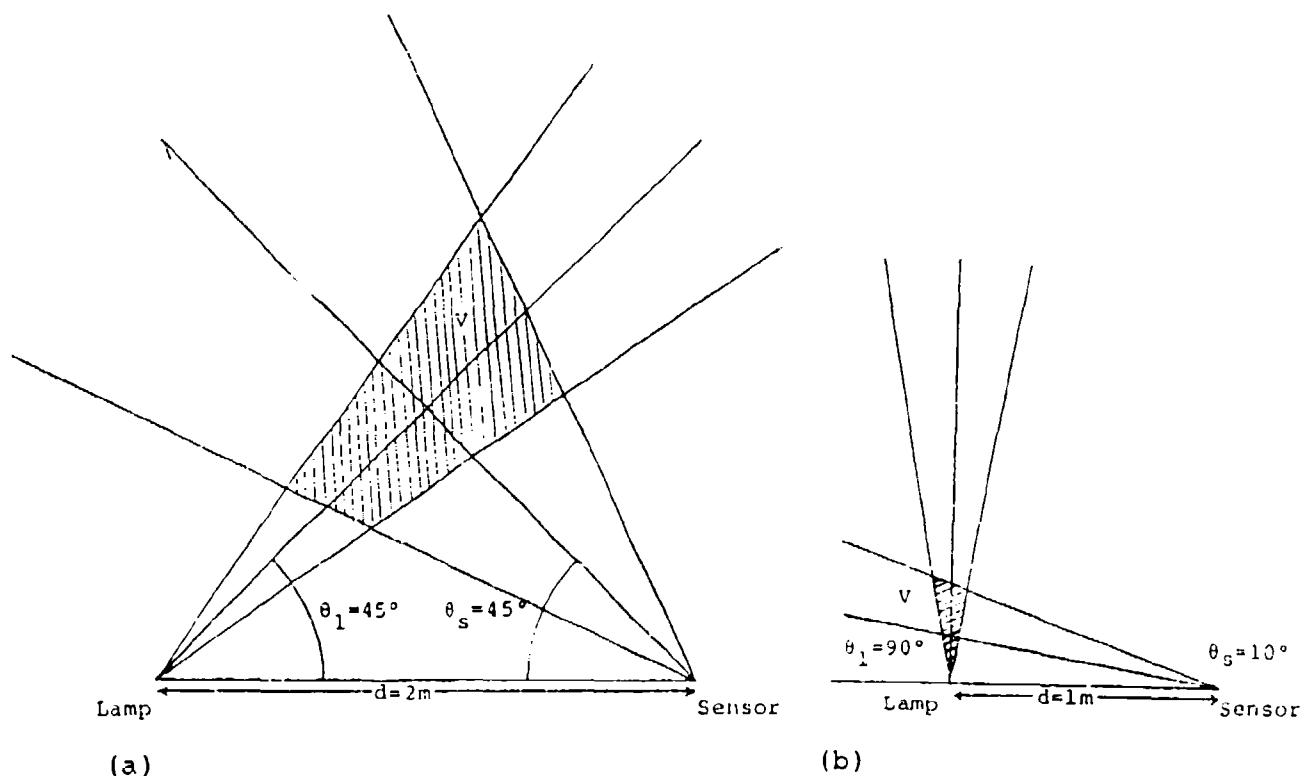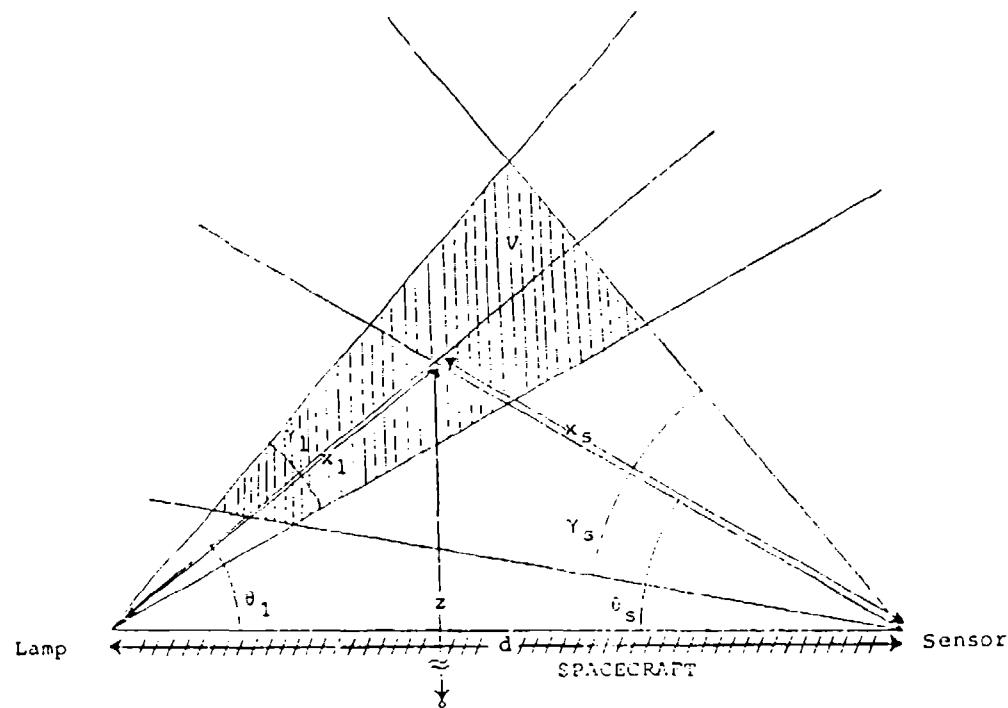
Figure 3. Excitation and viewing geometry. The symbols are explained in the text.

17

the lamp is

$$n_p = M_p/\Omega_1 cx_1^2,$$

where Ω_1 $(=2\pi[1 - \cos \gamma_1/2] \approx \gamma_1^2$ when γ_1 is small) is the solid angle of the cone and c is the velocity of light.

V is the "interaction volume" defined by the intersection of this light cone with the field of view of the optical sensor, as illustrated in Figure 3. The total rate R of (isotropic) emission of fluorescence photons from V is

$$R = Bc\sigma nn_p V.$$

The effective radiance I at the sensor, in energy units, is

$$I = E(\Omega_s a_s)^{-1} R \, p(x_s).$$

Here $E = 6.5 \times 10^{-19}$ joules is the energy of a 3064 A photon, $\Omega_s a_s$ is the etendue of the camera pixel or the photometer ($\Omega_s \approx \gamma_1 \gamma_s$ results from shaping to a rectangular field of view, as alluded to above), and $p(x_s)$ is the probability that a photon emitted at distance x_s from the sensor actually reaches its objective lens from angles within its field of view. $p(x_s) = \Omega_s/4\pi$ when the volume element V lies within the optical sensor's near field, and $p(x_s) = a_s/4\pi x_s^2$ when it is in the far field; the boundary is the hyperfocal distance of the camera or photometer $(a_s/\Omega_s)^{1/2}$. (This hyperfocal distance for lenses imaging objects at infinity onto the focal plane is more familiarly expressed as [focal length]^2/[aperture ratio]·[physical width of the pixel or slit]; I $\Omega_s a_s$ is the total power radiated by the hydroxyl radicals into the sensor aperture.)

Approximating the illuminating cone as square, we get for the interaction volume

$$V \approx (x_1 \tan \gamma_1)^2 (x_s \tan \gamma_s).$$

18

With the further approximation $\tan \gamma \approx \gamma$ (which is precise to 5% for $\gamma \leq 40°$), the radiance is then

$$I \approx E\sigma MM_p B \, (8\pi^2 a_s v_e z^2)^{-1} \quad X \quad \begin{cases} x_s \gamma_s & \text{(near field)} \\[2ex] a_s/x_s \gamma_1 & \text{(far field)}. \end{cases}$$

This expression for the measured radiance I applies when the linear dimensions of V are less than or comparable with the spacecraft radius z_0 (so that the water vapor density n is changing only slowly with z), and also to the distance x_s between V and the ultraviolet sensor. These two conditions hold for the two sample measurement scenarios that we treat below. (Should they not apply we could perform the straightforward, albeit tedious, integrations over the variations of n with z, and of p with x_s.)

This last expression shows that if the measurement volume V lies within the near field of the remote sensor the effective radiance increases linearly with both x_s and γ_s, because the volume sampled increases. (Note that the celestial (or atmospheric) background increases about linearly with γ_s but is independent of x_s.) When V lies beyond the hyperfocal distance this increase in sampled volume is more than offset by the larger range of the fluorescing source to the sensor.

Figure 4 shows the dependence of the dimensionless ratio $\eta \equiv x_s/d$ on the tilt angle $\theta_1(\theta_s)$ of the lamp (sensor) with respect to the spacecraft surface, which is taken as flat between the transmitter-receiver pair. (This approximation could be readily improved.) d is the separation of the lamp from the objective lens of the photometer or camera (Figure 3). The glow radiance is proportional (inversely proportional) to this ratio in the near (far) field.

It is clear from Figure 3 that η (and hence I in the near field) increases rapidly when the lamp and the sensor are almost

19
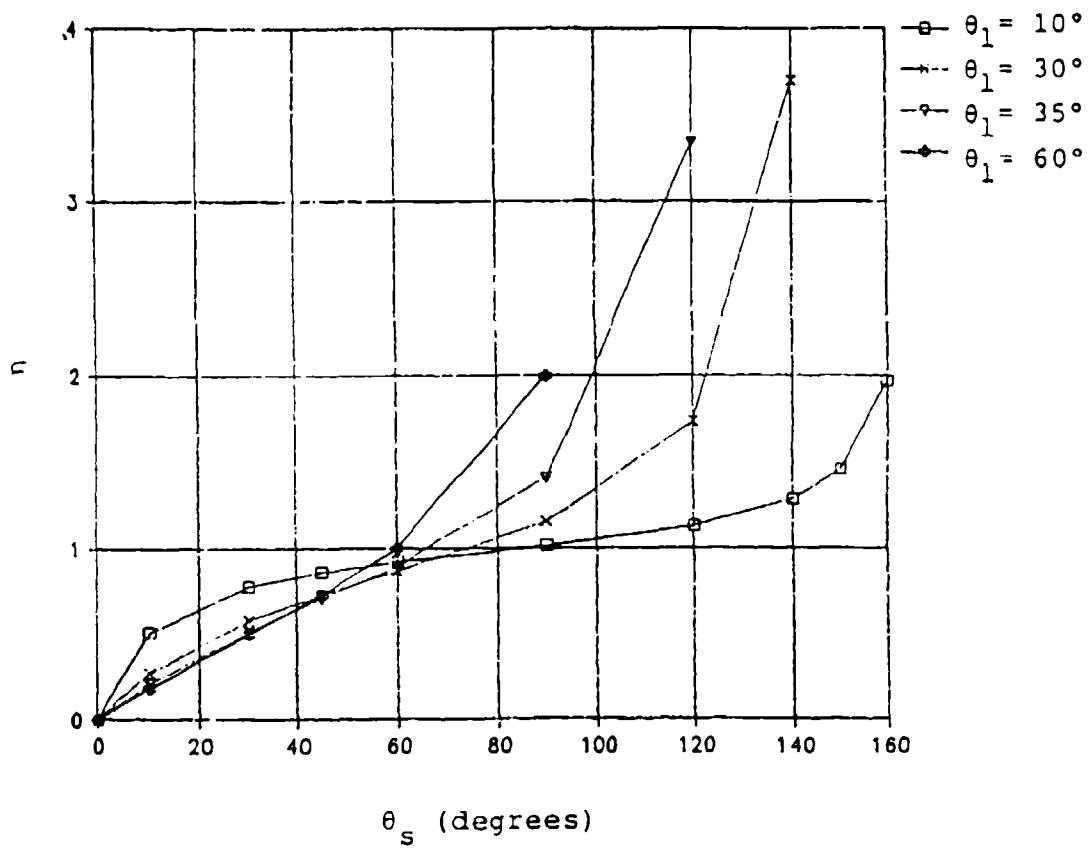
Figure 4.   Dependence of η on the transverse field
of the optical sensor

20

co-located and pointed in the same direction, as would be expected. However, in this near-collinear geometry most of the optical signal comes from the near field of the sensor, that is, the actual volume sampled lies very close to the spacecraft's surface. (The outward decrease in water density further reduces the total contribution from beyond about the first meter from this surface.) We estimated the measured glow radiances when the light "beam" and the photometer line-of-sight are essentially coaligned, and obtained results of only the same order of magnitude as those presented in the examples below.

Note also from Figure 4 that when θ_S is between 10° and 45° η is relatively constant at ~1 over the $30° \leq \theta_1 \leq 90°$ range of tilt angles of the photolyzing lamp. That is, the measured fluorescent radiance is insensitive to these parameters in this angular range, and in fact is also largely independent of whether the glow originates from the near or far field of the imaging sensor.

Example Water Vapor Measurements

We turn now to two specific scenarios of potential applicability for measuring water vapor concentrations near space vehicles. Case a) (Figure 3a) is designed to sample the outgassed water density "globally", i.e., over a roughly 1 m^2 spacecraft or rocket surface area, about 1 m above this surface; the result would be representative of the outgassing of H_2O molecules from a substantial fraction of the space vehicle's outer area. The parameters selected for this sample calculation are d = 2 m, θ_1 = θ_S = 45°, γ_S = 40° (as noted immediately above, the outcome is insensitive to the exact values of these distances and pointing angles). In contrast, case b) (Figure 3b) would sample only the "local" water density--i.e., outgassing from a ~100 cm^2 outer surface area--, about 20 cm directly above the lamp; it represents a virtually in situ measurement. The parameters selected for this latter scenario are d = 1 m, θ_1 = 90°, θ_S = 10°, γ_S = 20°.

When a wide-field AI/s camera is used as a single-channel photometer its hyperfocal distance $(a_S/\Omega_S)^{1/2}$ is $\leq$ 2 cm; thus the

21

glow volumes lie in the sensor's far field. Inserting the values above (and the parameters of Table 1) into the far-field expression for measured radiance yields

<div align="center">

Case a) $I = 8 \times 10^{-13}$ W/cm^2 ster,

Case b) $I = 3 \times 10^{-12}$ W/cm^2 ster.

</div>

The results differ by a factor ~4; we use the mean in the further calculations below. As expected, close-in projection intercepts provide higher UV signals, at the disadvantage of being less representative of the total outgassing of water vapor from the spacecraft or rocket.

Celestial Background

We next compare these apparent radiances with those of the night sky. Viewing in the zenith hemisphere from altitudes above the airglow layer (whose vertical spectral radiance from outside this layer is illustrated in Figure 1), zodiacal light and stars present the most intense near-UV background. The zodiacal light radiance is a minimum at the ecliptic pole, where it is closely approximated as scattered solar radiation at temperature 5500K with an emissivity $\epsilon = 5 \times 10^{-14}$ (Ref 13). As this zodiacal background is as much as 2 orders of magnitude higher than this figure in the ecliptic plane even at modest solar elongations, the water photolysis experiment should be designed so that the UV sensor points to high ecliptic latitudes.

The stellar background integrated over the 4π steradians of sky is equivalent to 460 zero magnitude stars (Ref 13). With the assumption that the spectral distribution is similar to that of our Sun--which is known to be an "average" star--, the mean radiance in the zenith hemisphere from the array of individual stars can be readily shown from Sun's 5500K effective temperature to be about 4×10^{-15} W/cm^2 ster A near 3064 A. (The experiment should also be planned to avoid pointing the sensor toward the galactic plane, where the density of ultraviolet stars is substantially higher.)

These astronomical backgrounds, normalized to the 55 A

response FWHM of the sensor, are summarized in Table 2. The signal from water photolysis [average of cases a) and b)] for the outgassing and active-measurement conditions that we have adopted is seen to be larger than both the noise equivalent radiance of the full wide-field AI/S detector array and the estimated mean background radiances from celestial sources.

Signal/Background Noise Ratios, Conclusions

Table 3 lists the ratios of signal to background expected for the range of water vapor desorption rates stated above. The noise from the background of individual stars is comparable with the mean background--on average, rather less than it--, and is of course specific to the pointing of the photometer's field on the celestial sphere (more on this immediately below). Widening (narrowing) the sensor field has the effect of suppressing (enhancing) noise spikes from individual UV stars. Both the average OH photolysis signal and the background (stellar + about-equal zodiacal) are taken from Table 2. The numbers in Table 3 refer to the full AI/S detector array--that is, the camera serves as a simple photometer, rather than an imager of the spatially-continuous ultraviolet glow. These figures show that coaddition of its pixels results in the integrated glow signal becoming large compared with the statistical (uncorrelated photon count) noise.

The following procedures would improve the signal-to-noise ratios in these measurements of off-vehicle water vapor densities.

1) Synchronous excitation and detection. The photolyzing UV lamp would be chopped at a frequency higher than the characteristic frequencies in the change in background as individual stars come into and out of the photometer field (which in general sweeps across the sky due to the spacecraft's angular motion). (If the sky background were time-stationary, a single comparison of lamp-on/lamp-off would provide the same ratio of signal to background noise.) This chopping frequency can be readily specified from the planned aspect angles of the spacecraft relative to the celestial sphere during flight and the glow

23

Table 2. Example Apparent Brightnesses

Source	Radiance ($W\ cm^{-2}\ ster^{-1}$)
Photolysis (mean of cases a) and b))	2×10^{-12}
AI/S NER (full array, 1-sec integration time)	2×10^{-14}
Stellar (averaged over the sky)	2×10^{-13}
Zodiacal (ecliptic pole, minimum --considerably higher in the ecliptic plane)	2×10^{-13}

Table 3. Signal/Background Ratios*

Water desorption rate M (gm/sec hemisphere)	3064 A band Signal/Celestial Background
0.006 (Ref 9)	1
0.03 (Ref 8)	5
0.2 (Ref 10)	35

---

*Average of measurement cases a) and b) in Figure 3, all pixels summed.

24

measurement geometry.

The photoelectron signal N_s from the detector is

[Radiance] x $[a_s\Omega_s]$ x

[Transmission of the wavelength-isolating filter] x

[Quantum yield of the photocathode] x [Integration time].

With the previously-adopted M = 0.03 gm/sec this signal is $[(2 \times 10^{-12})/(4 \times 1.6 \times 10^{-19})]$ x [0.3 x 0.1] x [0.2] x [0.2] $\approx$ 4000 counts in one second. The corresponding background N_b is 800 counts. We would therefore expect statistical signal-to-noise ratios equal to $N_s/(N_s + 2 N_b)^{1/2} \approx$ 54 in two seconds integration time from "ideal" synchronous detection. (We have neglected the dark counts from the noise equivalent radiance of the instrument itself; refer again to Table 2.) Water vapor desorption rates of ~0.001 gm/sec should thus be detectable in a few seconds integration time, with AI/S-scale instrumentation used in "photometer" mode. Note, however, that the threshold sensitivity of single 3 x 3 pixels-elements of the AI/S is about 2 orders of magnitude higher than the full parallel-operated array, and thus imaging the glow becomes practical only at correspondingly higher water desorption rates.

2) Use of longer integration times. There is no obvious reason to preclude hundreds- or even thousands-seconds measurement periods.

3) Processing of the image from the focal plane array, to subtract (at least the brighter) individual resolved stars from the scene. (The water density measurement presents the reverse of the usual DoD problem of distinguishing discrete targets from spatially-continuous background glows: the excitative-photolysis volume is to be quantified against a background of point sources.) A capability for optimal extraction of scene information is a definite advantage of potentially "smart" focal plane arrays such as the AI/S. Specifically, the image processing could be carried out automatically using algorithms that recognize discrete sources of radiation, or in which the star field is preprogrammed. Alternatively, individual stars could be edited out manually from

frames projected onto a video screen before all the photocurrents from the scene are coadded. This manual noise suppression could be supported by visible light images of the star field taken by a coaligned AI/S camera, which identify those pixels onto which stars image.

Single-channel photometers have the advantages of low cost and simplicity of operation, as well as somewhat better threshold sensitivity than coadded AI/S-camera focal planes (because they are not subject to thermal noise from the semiconducting diode array behind the image-intensifying photocathode). The disadvantages of simple multiplier phototube-based instruments relative to electronic cameras include less protection against the false background from very bright individual stars, and less scope for shaping the field of view to enhance the photolysis-emission volume against the celestial scene. In sum, photometers having about the same etendue as the coadded AI/S would be able to measure the same low concentrations of outgassed water vapor, albeit with less "reliability"; refer to Table 4.

Implementation

Measurement from onboard spacecraft of "close-in" or globally-averaged" water vapor concentrations by this ultraviolet photolysis method requires the following further effort before actual hardware is assembled.

-- Specification of the relative aperture, shape of the angular field, and response uniformity over this field of view of the photometer or camera.

-- Specification of the transmission characteristic of the optical filter (and photocathode type; refer to the discussion in Section 1) that isolates the OH A $\rightarrow$ X 0,0 band from background radiations.

-- Space qualification of a vacuum-ultraviolet resonance lamp.

-- Design of the projection of the fields of this illuminating lamp and the photometer/camera on one another. (As shown above, the signal/noise ratio achieved generally decreases

26

with the area of outgassing surface probed.
-- More accurate calculation of the response of the photolyzer-sensor pair to given concentrations of water vapor, that is, absolute <u>calibration</u> of the measurement system.
-- Development of a doctrine for timing (photolyzing lamp on-off) and pointing (sensor field away from the galactic and ecliptic plane and individual bright UV stars), to suppress the celestial background.

Table 4.   Sensor Characteristics

Feature	Photometer	Intensified Detector Array (AI/S)
Cost	Low	High
Complexity, Weight	Low	High
Image Processing Capability (Star identification/subtraction, field of view limiting)	No (but fov could be shaped)	Yes
Dark Noise	Very low	Low
Availability	To be built	On hand

RELATION OF THE COMPOSITION OF SPACECRAFT-CONTAMINANT PARTICLES
TO THEIR SCATTERING AND EMISSION SPECTRA

Problem Statement

Spaceborne particulates near manned vehicles (such as Shuttle
Orbiter) with average diameters ~3-300 μm have been observed
photographically and even visually, as well as by other means.
The radiations scattered from and emitted by them degrade
performance of optical sensors for surveillance and measurement of
atmospheric/celestial backgrounds, and the physical contamination
also interferes with operation of other spacecraft systems. The
chemical composition of these particles, along with their size
distribution--measurable as described immediately below--, would
serve to identify their origin(s) and thus lead to improvement of
the orbital environment.

Approach, Caveat

The spectral reflectivity--"color"--of microns-size particles
illuminated by the sun and atmosphere, and its dependence on
angle, provide the same semiquantitative information about their
composition as do these optical properties of macroscopic objects.
Similarly, the scattering of infrared earthshine and thermal
radiation from particulates is a function of the (wavelength-
dependent) complex index of refraction and thermal diffusivity of
the material of which they are composed.

The relationship between these optical parameters and
chemical composition (and even crystal structure) is not unique,
or necessarily predictable from theory; and furthermore the
signal/noise in measurements of particle spectra from onboard
spacecraft is typically low. In consequence, calculations
specific to the expected materials and instrument capabilities are
needed to assess the practicality of identifying the sources of
contaminants off spacecraft from their spectral distributions.

Technical Background

Spectra of the scattered and thermal radiation from particulates can in principle be determined by imaging with multiple filter cameras, or by the more obvious conventional and slitless spectroscopy. The procedure follows directly from that used to measure their total sunlight-scattering cross-sections and distances from the spacecraft (and their velocities), which we applied previously to silver halide photographs taken on an early shuttle mission (Ref 14). This method is briefly outlined here to provide a pragmatic background for assessing its applicability to identifying types of particulate materials. (Refer also to the detailed theoretical treatments of optical scattering from small particles in texts such as Ref's 15 and 16.) The gray-body infrared emission spectra of particulates are subject to essentially the same physical principles as the visible and near-ultraviolet (sunlight-scatter) radiations.

As most if not all of the particles that are optically characterizable by spaceborne instruments have circumferences large compared with the wavelengths of the photons (the size parameter in theoretical treatments of spherical shapes is 2π [radius]/[wavelength]), the complexities of Mie interference that lead to the well-known strong oscillations in the differential and total scattering cross-sections at smaller effective radii are absent. Further, as experience shows, most individual particles that provide above-threshold spectral signal/noise ratios lie inside the hyperfocal distance of imaging sensors--$(a_s/\Omega_s)^{1/2}$, as defined in Section 2, or in a practical sense (diameter of the objective lens)/(angle subtended at this lens by one resolution element of the photographic film, or pixel of the photodiode array, or slit width of the spectrometer). For surveys with cameras of the space immediately surrounding spacecraft this distance is of order 20 m. The particles within this range are "out of focus", with the result that

-- morphological detail on these particles is not (or is very

poorly) resolved, and

-- the area of the blur spot in the image plane varies with (particle range)$^{-2}$.

That is, snapshots of stationary (with respect to the vehicle) spaceborne particulates that lie inside the hyperfocal distance carry essentially no information about their shape or texture; their distance from the remote sensor can (at least in principle) be measured from the absolute dimensions of their image; and their velocity components can be determined from these ranges and the position of the centroid of the blur spot in sequential frames, or even from a single time exposure (from the angular length and absolute widths of the extended image streak).

The mean irradiance within this image area is a much more complicated technical issue, as it requires detailed Fresnel's Law-based computations of the reflection-refraction-absorption of light rays incident over the surface of the particle. If the particle has an irregular shape and is tumbling with a period less than a few times the measurement interval, this irradiance will vary quasi-regularly: the image will blink due to what may be termed near-specular reflections, which strongly indicates that the object is a solid. But since not all non-spherical or inhomogeneous solid particles have short-period rotational motions, solid materials broken off Orbiter surfaces would not be inherently distinguishable from liquid droplets (which surface tension forms into nearly perfect spheres, particularly in the gravity-free environment). Thus repetitive modulation of exposure in the image plane ("flickering") is a sufficient but not necessary condition for material in the solid phase--a fleck of dried paint, for example.

This irradiance in the image is approximately (see Ref 15 or 16)

--(particle "radius")^2 X
Σ[(irradiance incident from each solid angle) X
(angular scattering function)].

30

Note that the irradiance in the plane of photodetectors focused at infinity in object space does not depend on the range of the particle [when it lies within the hyperfocal distance]. The "scattering function", which depends (usually strongly) on the angle between the vectors from the scattering center to the element of solid angle from which illumination arises and to the objective lens of the sensor, is in effect the fraction of all of the incident photons that emerge per unit solid angle. (It can be viewed as [irradiance out/irradiance in] normalized to 4π steradians. A similar definition holds for thermally- (self-) radiating particles.) This function quantifies the departure from isotropic re-radiation that results from reflections at the surfaces of the particle and refraction-absorption within it; these quantities in turn depend classically on the real and imaginary components of the material's refractive index. (We restrict the discussion here to homogeneous paraticles, and further assume relatively regular shapes.) The wavelength dependence of this complex index of refraction is the basis for discrimination among particle compositions (and crystal structures) using the spectral distributions of their scattered (and emitted) optical radiation.

Attached for reference in Figure 5 is this scattering function for droplets of water (real index = 1.33, imaginary $\approx$ 0.00) that are large compared with the light wavelength. The mean irradiance in the blur spot from directly sunlight-illuminated spherules, and thus in first approximation their projected area when their composition and therefore refractive index are known, can be seen to depend (strongly when the indexes are low) on angle to the sun. This solar disk subtends about 7×10^{-5} steradians near the earth; at the same time spaceborne particles are also illuminated, over almost 2π steradians, by the sunlight photons that are scattered from the atmosphere and the earth's surface. This diffuse source produces roughly a quarter as much visible flux at spherical objects as direct sunlight (and quite obviously

31
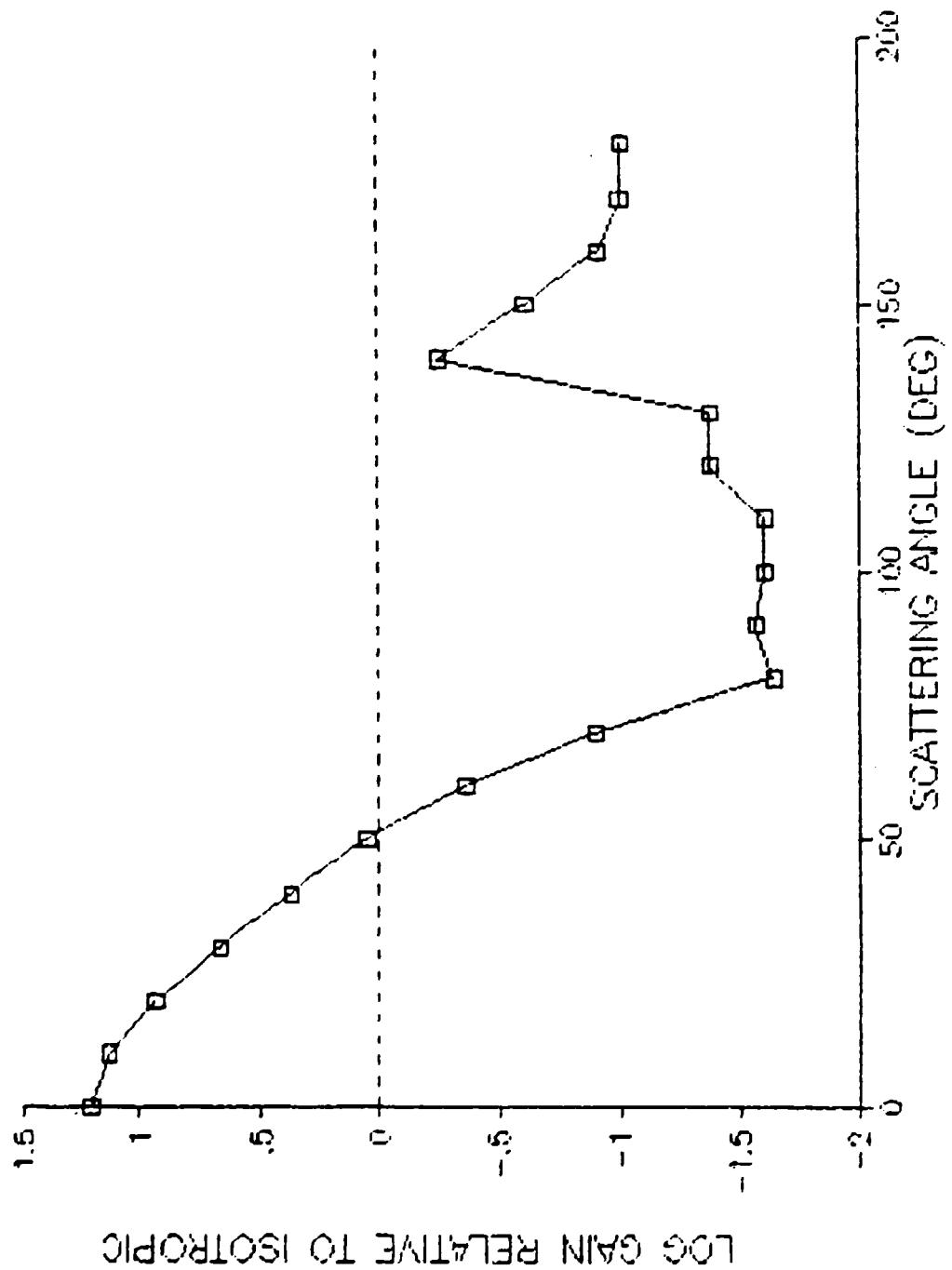
Figure 5. Photometric function of a water droplet of circumference large
compared with the light wavelength expressed as gain factors
relative to isotropic scatter.

32

more when the vehicle passes over large snow-covered areas than cloudfree smooth oceans, which have low albedo). Particulates near spacecraft would also be illuminated by sunlight and earthlight reflected from the body.

These photons coming from other than the direction to the sun have the effect of damping the angular dependence shown in Figure 5, were this dependence interpreted as due solely to the direct sunlight. They also reduce the "contrast" in sequential images of tumbling nonspherical particles. We note also that the wide range of angles of earthshine illumination would play a part in measurements of particle indexes of refraction from the variation in relative image irradiance as they move across the camera's field of view, during which period the angular scattering function of direct sunlight can be undergoing large changes. This method for particle characterization from onboard spacecraft, which while related to laboratory nephelometry has not to our knowledge been previously proposed, complements the measurement of wavelength dependence of refractive index reviewed here.

Virtually all contaminant particles outside the ~20,000,000-μm hyperfocal distance of the imaging system subtend angles smaller than one pixel, and thus are also--like stars--spatially unresolved. The irradiance at the camera lens produced by such distant objects again depends on their angular scattering function, but the apparent mean irradiance within the resolution element of the sensor in this case varies with $(\text{range})^{-2}$ X $(\text{"radius"})^{+2}$.

Infrared Spectral Imaging

The scattering of infrared earthshine by particulates follows the same physical principles as the scattering of visible (and near-infrared, and ultraviolet) solar photons. Small particles also act as thermal emitters, at a temperature that is determined by their absorption and re-emission of sunlight and the radiations from the atmosphere, and also their thermal diffusivity (which in large part controls their temperature structure). The spectral

33

intensity also depends on the dimensions of the particle relative
to the wavelength; that is, small particles can be considered to
be "antennas" (in an electromagnetic-theory sense), rather than
macroscopic gray bodies (see for example Ref 16). The spectral
emissivity and absorptivity in multiple-bandpass images or
dispersed infrared spectra provide a quantitative measure of the
dependence of index of refraction on wavelength.

The inverse problem is treated by the CHFPROG subroutines of
the U. S. Army's Optical Signatures Code (Ref 17; other such
models also exist), which provides a detailed numerical procedure
for practical calculations of the infrared sterances from "chaff"
particles of specified dimensions and index of refraction.
(Recipes are also given for some non-spherical shapes.) The
sample scaled spectral radiances and compilations of refractive
indexes for 50-odd materials are particularly useful features of
this backgrounds model. Information from the Optical Signatures
Code can be directly applied in calculating the wavelength
dependences of the irradiances from--i.e., infrared signatures of
--off-vehicle contaminant particles that have the chemical
compositions expected from their suspected source.

Practical Considerations

Experience with earlier images of discrete contaminants in
the vicinity of Shuttle Orbiter (Ref 14) indicates that particles
with radii down to about 2 μm that lie within a 20-m hyperfocal
distance at small solar-scattering angles would be above the noise
threshold of unintensified fast polychromatic photographic film
cameras exposed to the full spectrum of sunlight. (Smaller-size
particulates must of course also be present near the spacecraft.)
We also found that the signal above inherent photodetector noise
and the celestial background decreases with increasing transverse
component of the particle's velocity, as would be expected for
silver halide films in particular (which respond nonlinearly) as
well as for other focal planes (such as photodiode arrays). With
the further assumption that absorption of visible light by the

34

particles was small (i.e., they have low imaginary index component), most of their radii turned out to be in the 5-25 μm range. Use of intensification in the image plane would be expected to lower the minimum detectable irradiance by at least an order of magnitude, although in practice we have not found such a sensitivity improvement in electronically intensified images of star fields.

Figure 6 shows the spectrum of direct sunlight with the nominal long-wavelength cutoffs of photoelectric/photographic and near infrared-sensitive silicon faceplates. (The AI/S employs some Si diode detectors; the solar flux in the UV is too low to allc/ the present UV channels of this instrumnent to image off-vehicle particulates.) The particle size data referenced just above, taken with the predicted improvement in threshold sensitivity of image intensifiers, indicate that high light grasp sensors could isolate about ten discrete wavelength intervals on sunlit ~10's μm particles near spacecraft. Whether the spectrum of scattered light from these particles is dispersed by a conventional spectrometer or with the object serving as its own slit, or sampled in limited wavelength intervals by an array of filter cameras, is immaterial [when these sensors have the same effective aperture ratio]: only enough photons are available to compose roughly ten independent images of the particle in single exposures. Note that individual filter-image frames can be exposed for only a time short compared with the tumbling or "distancing" time of the particle(s), lest the changes in total irradiance be confused with spectral variations. (The narrow angular field of conventional spectrographs in the direction of their slit width limits their applicability for surveys.)

We have identified no similar infrared image data that provide practical estimates of the count rates of contaminant particles off spacecraft. However in view of the argument that LWIR cameras with very large apertures have the capability to track thermally-emitting ~$(1-m)^2$ cross-section objects at ~1000 km ranges, $(100-\mu m)^2$ particles at 5×10^{-3}-km ranges could be

35
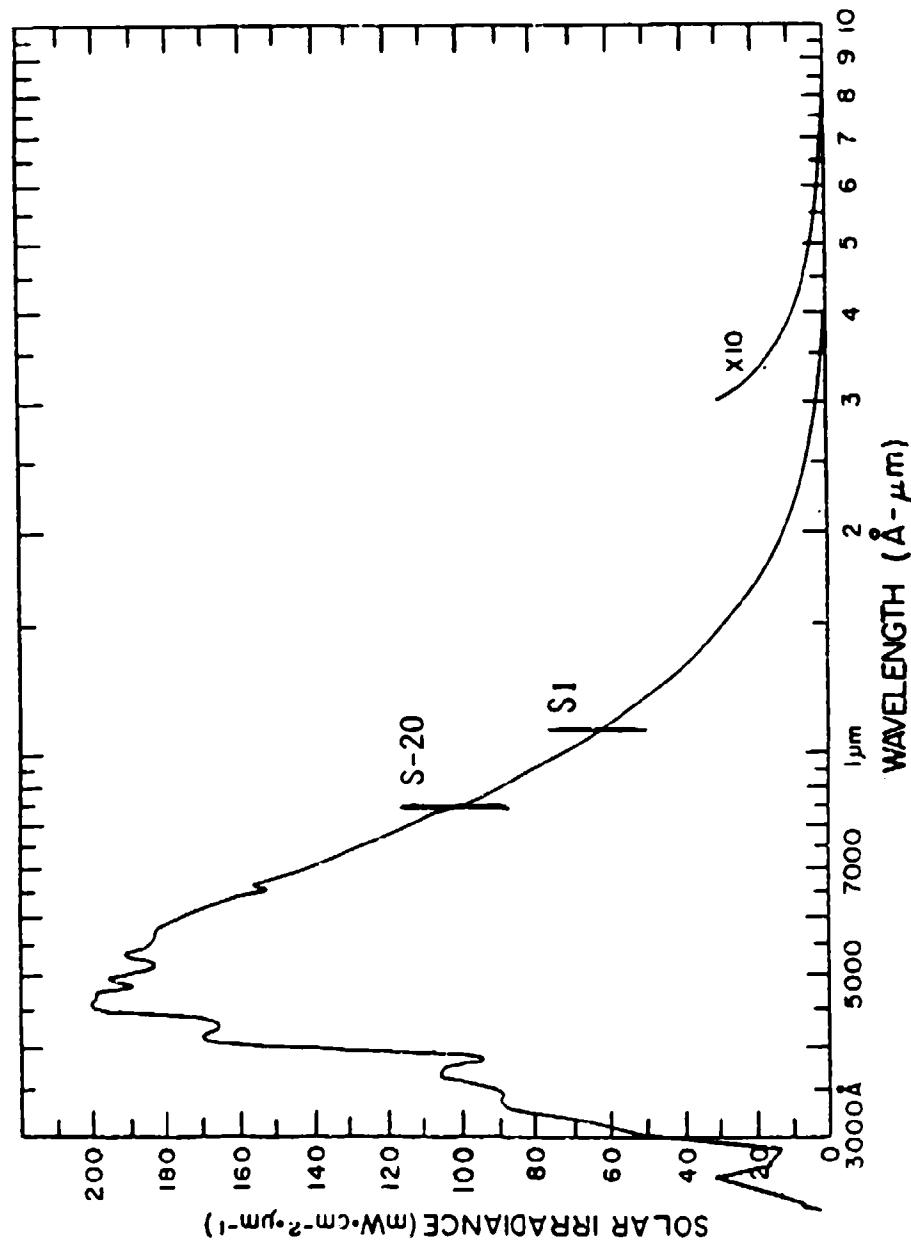
Figure 6. Solar spectral radiance and long-wavelength "cutoff" of S-20 photomultiplier cathodes and Si photodiodes.

36

expected to be above the noise thresholds of much smaller-scale IR radiometers. (As noted above, when the object is outside the hyperfocal distance its irradiance depends on (range)$^{-2}$). In any case, the signal/noise that would be provided by infrared cameras of known light grasp lends itself to direct calculation using (for example) the Optical Signatures Code, which would allow the IR spectral resolutions achievable by such cameras to be estimated.

Particle Composition

The background material above provides a basis for addressing the question of how the refractive indexes of spaceborne particles would be derived from spectra or multiple radiometrically-calibrated images, and--the critical issue--how the chemical composition of these particles can be determined from the dependence on wavelength of this complex index of refraction.

We judge that the most effective approach is to work backward from handbook values of the indexes of those materials from which the particulates are expected to be composed, to fit the resulting spectral distributions to those measured by onboard sensors. The concept, then, is to start with the dependence on wavelength of the spectral irradiances from sets of particles having given effective radii, and that have candidate crystal structures and chemical compositions (water, fluorocarbons, Florida beach or California desert sand, and those of Shuttle Orbiter's protective tiles, insulation and thermal blankets, paints, and other construction materials); then to convolve these spectral distributions with the response of existing and projected spacecraft instruments; and then to compare the predicted spectra with those actually measured. The complex indexes of refraction of most if not all of these candidate substances are already known, and the others can be readily measured. Fitting these synthetic spectra to the preceivedly low-resolution spectrum distributions provided by real spacecraft instruments is conceptually the same process often applied in identifying other sources of atmospheric radiation (excited molecules and atoms in

37

auroras, for example, or nuclear explosions), and of course also in many laboratory situations.

Systematic such calculations would assess tne spectral "contrast" of contaminant particulates with suspected compositions, and--comparably important--determine the wavelength resolutions and absolute sensitivities required for effective discrimination among them. In sum, the next step in evaluating the usefulness of the concept described here for remote optical identification of the particles in the spacecraft environment is production of a synthetic database of spectral sterances of model (assumed-spherical and -homogeneous) such particles for estimating the signal-to-noise ratios in spectral image data from botn existing (for example, the AI/S fitted with photodetectors sensitive to sunlight) and dedicated spectrometers and cameras.

REFERENCES

1. I. L. Kofsky, J. L. Barrett, T. E. Brownrigg, P. J. McNicholl, N. H. Tran, and C. A. Trowbridge, Excitation and Diagnostics of Optical Contamination in the Spacecraft Environment, AFGL-TR-88-0293 (01 July 1988). ADA 202429

2. J. L. Kulander, H_2O rotational line emission between 10 and 50 μm due to collisions with O, J. Quant. Spect. Rad. Trans. 16, 21 (1976).

3. C. E. Kolb and J. B. Elgin, Classical calculations of NH_3 and H_2O rotational excitation in energetic collisions with atomic oxygen, J. Chem. Phys. 66, 119 (1977).

4. K. S. Tait, C. E. Kolb, and H. R. Baum, Classical calculations of rotational and vibrational excitation in energetic atom-diatomic hydride collisions, J. Chem. Phys. 59, 3128 (1973).

5. A. S. Jursa (ed.), Handbook of Geophysics and Space Environments, (1985), AFGL-TR-85-0315. ADA 167000

6. F. X. Kneizys, E. P. Shettle, W. O. Gallery, J. H. Chetwynd, L. W. Abreu, J. E. A. Selby, S. A. Clough, and R. W. Fenn, Atmospheric Transmittance/Radiance: Computer Code LOWTRAN 6, AFGL-TR-83-0187 (01 Aug 83). ADA 137786

7. A. L. Broadfoot and K. R. Kendall, The airglow spectrum, 3100-10,000 A, J. Geophys. Res. 73, 426 (1968).

8. H. Okabe, Photochemistry of Small Molecules , Wiley, New York (1978).

9. S. J. Young and R. R. Herm, Model for radiation contamination by outgassing from space platforms, J. Spacecraft Rockets 25, 413 (1988).

10. E. Wulf and U. von Zahn, The shuttle environment: Effects of thruster firings on gas density and composition in the payload bay, J. Geophys. Res. 91, 3270 (1986).

11. D. G. Koch et al., Infrared observations of contaminants from Shuttle flight 51-F, Adv. Space Res. 7, 211 (1987).

12. A. A. Radzig and B. M. Smirnov, Reference Data on Atoms,

<u>Molecules, and Ions</u>, Springer-Verlag, Berlin (1985).

13. C. W. Allen, <u>Astrophysical Quantities</u>, Oxford, New York (1963), p. 235.

14. D. Smith et al., Optical/particulate contamination during on-orbit space shuttle operations, Paper at AIAA Meeting on Shuttle Environment and Operations (31 Oct-02 Nov 1983).

15. H. C. van de Hulst, <u>Light Scattering by Small Particles</u>, Dover, New York (1981).

16. C. F. Bohren and D. R. Huffman, <u>Absorption and Scattering of Light by Small Particles</u>, Wiley, New York (1983).

17. [U. S. Army] Optical Signatures Code, SD83-BMDATC-2641 (1983).